Facile Synthesis of CuFe$_2$O$_4$/CuO-Ti$_3$C$_2$T$_x$ Composite for Supercapacitor Electrode Material

By

Khadija Tul Kubra

(Registration No: **00000402980**)

A thesis submitted to the National University of Sciences and Technology, Islamabad,

in partial fulfillment of the requirements for the degree of

Master of Science in

Chemistry

Supervisor: **Dr. M. Adil Mansoor**

Co supervisor: **Dr. Numan Arshad**

School of Natural Sciences

National University of Sciences & Technology (NUST)

Islamabad, Pakistan

THESIS ACCEPTANCE CERTIFICATE

Certified that final copy of MS thesis written by **Khadija Tul Kubra** (Registration No. **00000402980)**, of **School of Natural Sciences** has been vetted by undersigned, found complete in all respects as per NUST statutes/regulations, is free of plagiarism, errors, and mistakes and is accepted as partial fulfillment for award of MS/M.Phil degree. It is further certified that necessary amendments as pointed out by GEC members and external examiner of the scholar have also been incorporated in the said thesis.

Signature: _____

Name of Supervisor: Dr. M. Adil Mansoor

Date: _____29/08/2024_____

Signature (HoD): _____

Date: ___29/08/2024___

Signature (Dean/Principal): _____

Date: ___02.09.2024___

National University of Sciences & Technology

MS THESIS WORK

We hereby recommend that the dissertation prepared under our supervision by: Khadija Tul Kubra, Regn No. 00000402980 Titled Facile Synthesis of CuFe2O4/CuO-Ti3C2Tx Composite for Supercapacitor Electrode Material be Accepted in partial fulfillment of the requirements for the award of MS degree.

Examination Committee Members

1. Name: PROF. MUDASSIR IQBAL   Signature: _____

2. Name: PROF. AZHAR MAHMOOD   Signature: _____

Supervisor's Name DR. MUHAMMAD ADIL MANSOOR   Signature: _____

Co-Supervisor's Name DR. NUMAN ARSHID   Signature: _____

_____
Head of Department

29/08/2024
Date

COUNTERSINGED

Date: 02·09·2024

Dean/Principal

<u>DEDICATION</u>

To my amazing parents, whose love, guidance, and sacrifices have shaped who I am today. Your unwavering belief in me has been my greatest source of inspiration. Thank you for always being there, offering your support, encouragement, and a listening ear whenever I needed it. Your love has been the constant light that has guided me through the challenges and triumphs of this academic journey. I am eternally grateful for your sacrifices, for your constant belief in me, and for your unconditional love. This thesis is dedicated to you, with all my love and gratitude.

ACKNOWLEDGEMENTS

Contents

LIST OF FIGURES

ABSTRACT

Energy generation from renewable energy assets is beneficial to overcome the energy crises. The efficient development of electrochemical cell and electrochemical energy storage devices is crucial for this purpose. In this research, the synthesis of $CuFe_2O_4/CuO$, $Ti_3C_2T_x$ and $CuFe_2O_4/CuO$-$Ti_3C_2T_X$ composite is reported. The composition, morphology and structure of synthesized material was confirmed by XRD, Raman, FTIR and SEM . The Electrochemical measurements indicate that $CuFe_2O_4/CuO$-$Ti_3C_2T_X$ composite exhibited highest specific capacitance 1779 F/g at 1A/g current density at 0.46 V vs Ag/AgCl potential as compared to pristine $Ti_3C_2T_x$ (1060 F/g at 1 A/g C.D) and $CuFe_2O_4/CuO$ (1026 F/g at1 A/g C.D). The hybrid composite $CuFe_2O_4/CuO$-$Ti_3C_2T_X$ was stable and maintained the capacitive retention of 97.3% and coloumbic efficiency of 98.9%. This indicated the successful synthesis of material $CuFe_2O_4/CuO$-$Ti_3C_2T_X$ for electrochemical energy storage application.

Chapter 1

INTRODUCTION

Today's society requires extensive energy storage solutions to meet the needs of residential, public, and industrial sectors on a grand scale. Consequently, there is a heightened focus on energy storage technologies owing to superior storage capacity, rapid charge and discharge capabilities, elevated levels of rechargeability, and versatility in various applications [1].

Since the early 20th century, the demand for energy has surged due to population growth and economic expansion. Moreover, the drive towards rapid industrialization and the pursuit of advanced technologies have escalated the need for more energy sources. This surge in demand has led to a significant increase in the consumption of fossil fuels, hastening their depletion and contributing to energy security concerns, environmental pollution, and global warming [2]. The urgent need for energy has taken research into alternative energy solutions and the development of energy storage systems. Storing energy electrochemically is heralded as a pivotal breakthrough among all energy storage and conversion technologies [3].

The global enthusiasm, momentum, and substantial investments in energy production are crucial for facilitating the transition away from today's energy economy that is completely dependent on fossil fuels, especially in electricity generation. However, the intermittent nature of most renewable energy sources poses a challenge to efficient electricity generation and widespread adoption [4].The decentralized distribution of renewable energy offers significant advantages in minimizing the economic and environmental costs associated with centralized power transmission. In economically disadvantaged and developing regions, where many communities face a lack of electricity and basic amenities, renewable energy plays a critical role. In these areas, the adoption of renewable energy can spur economic development and substantially improve living standards [5].

Production of green energy encompasses the generation of energy from wind, solar, biomass, and hydropower sources. Electrochemical energy forms a crucial segment of the clean energy range. Fuel cells and supercapacitors represent alternative energy sources that function based on the principle of electrochemical conversion [6].
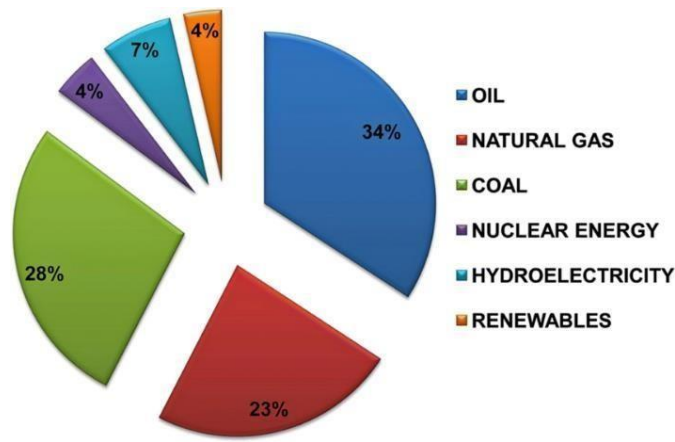
Figure 1 Sources of energy

1.1 Electrochemical energy storage devices (EES):

Electrochemical energy storage (EES) technology is a method that allows the transformation of electrical and chemical energy into a stored form, which can be released through chemical processes [7].

1.2 Categories of ees systems:

Electrochemical energy storage is among the most established methods for storing energy in power systems and is broadly divided into three main types:

1. Primary batteries

2. Secondary batteries

3. Fuel cells

1.2.1 Primary battery or cell:

A primary battery, also known as a primary cell, is a single-use battery (a type of galvanic cell) intended to be disposed of after its life cycle ends, unlike a secondary cell (rechargeable battery) which is designed for multiple uses through recharging. Typically, the chemical reaction that occurs within the cell is irreversible, making the cell not suitable for recharging. As the battery is utilized, the chemical components that facilitate power generation are depleted, leading to the cessation of electricity production. These cells are often referred to as dry cells due to the absence of liquid components.

1.2.2 Secondary battery or cell:

Secondary batteries function by storing energy chemically and converting it back to electrical energy when needed. During the charging process, energy is introduced, prompting an electrochemical alteration in the cell. This allows the battery to be discharged, reversing the electrochemical changes and enabling them to proceed spontaneously. The chemical substances produced during the charging phase facilitate electrochemical reactions that: (i)

release electrical energy, (ii) revert the system to its original state. A commonly known example of a secondary battery is the lead-acid battery found in vehicles, which consists of porous lead and porous lead dioxide electrodes immersed in a concentrated sulfuric acid electrolyte[8].
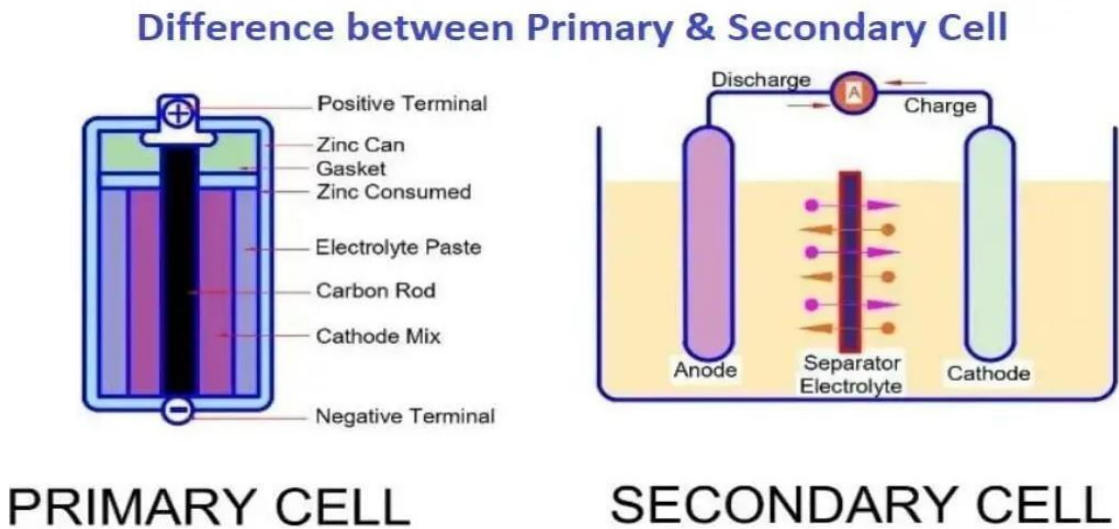
Figure 2 mechanism of primary & secondary cell

1.2.3 Fuel cell:

As A fuel cell functions as an intricate electrochemical apparatus that converts the chemical energy derived from a fuel, often hydrogen, alongside an oxidizing agent, predominantly oxygen, into electrical energy through a series of oxidation-reduction reactions. Contrary to the majority of batteries, which encase all requisite chemicals for energy generation internally, fuel cells necessitate an uninterrupted influx of fuel and oxygen (frequently sourced from ambient air) to perpetuate the reaction.

Fuel cells possess the capability to produce electricity continuously provided there is an ongoing supply of fuel and oxygen. They have an anode, a cathode, and an electrolyte that facilitates the transference of ions, typically hydrogen ions (protons), throughout the cell.

Within the anode's domain, a catalyst initiates fuel's oxidation reactions, engendering ions (commonly hydrogen ions) and electrons. These ions traverse the electrolyte from the anode towards the cathode, whereas electrons journey through an external connections from the anode to the cathode, engendering a stream of direct current electricity.

At the cathode, a distinct catalyst aids in the reaction among ions, electrons, and oxygen, culminating in the generation of water and, occasionally, additional byproducts [9].
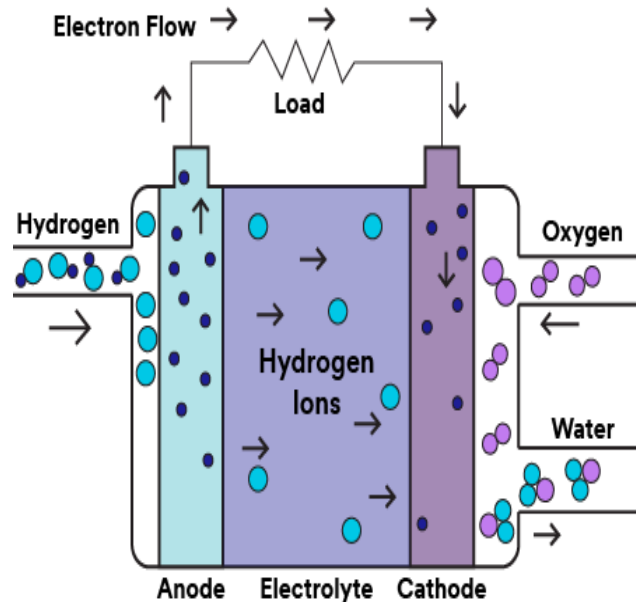
Figure 3 Mechanism of Fuel cell

1.3 Supercapacitor:

The surge in renewable energy sources, predominantly supplied as electric power, has underscored the need for dependable electrochemical storage systems such as batteries, fuel cells, and electrochemical supercapacitors (SCs). Among these, SCs have garnered increased interest over batteries due to their superior rapid charging capabilities (for instance, SCs can discharge in 1–10 seconds compared to 10–60 minutes for lithium-ion batteries) and their greater cycle life (SCs can exceed 30,000 hours versus batteries which typically last for over 500 hours).

Despite their lower energy density, recent developments in SC technology, particularly in electrode materials and electrolytes, show promise in bridging the performance gap between traditional batteries, fuel cells, and existing capacitor technologies [10].

1.3.1 What are Supercapacitors?

 Supercapacitors are advanced energy storage devices that accumulate charge through electric double-layer capacitance and pseudocapacitance mechanisms. Contrary to traditional capacitors that store charge by separating it across a dielectric material, supercapacitors electrostatically store energy on electrode surfaces. This results in a high power density and the ability to charge and discharge quickly, making them well-suited for applications needing quick bursts of power and frequent cycles, like regenerative braking in electric vehicles, peak power shaving in renewable energy systems, and capturing energy from sporadic sources.

The major disadvantage to supercapacitors is their low energy density, or Ed. Because the Ed of capacitors is directly proportional to the square of the voltage, V, and capacitance, Cs, an increase in Ed requires an increase in Cs or V—or both. This improvement may be achieved

by using electrode materials with high Cs, electrolytes with big potential windows, and careful optimization of the integrated system design. The individual parts of supercapacitors, such as electrode materials and electrolytes, can be rather easily constructed, but good synergistic performance is usually only obtained if the pore dimensions and configuration of the electrode material match the size of the electrolyte ions. Some main features, including but not limited to conductivity, power density (Pd), and operating temperature spectrum, are largely defined by electrolytes/solutions.

1.3.2 Types of Supercapacitors

Supercapacitors are categorized into three main types:

1.3.2.1 Electrostatic Double-Layer Capacitors (EDLCs):

These capacitors consist of two electrodes, a separator, and an electrolyte with dissolved positive and negative ions. The electrodes, often made from carbon or its derivatives, exhibit high electrostatic double-layer capacitance. The charge separation in EDLCs is minimal, typically ranging from 0.3 to 0.8 nm.

1.3.2.2 Pseudocapacitors:

This type of supercapacitor is used less often and is offered commercially by a small number of manufacturers. From an operating principle standpoint, they are more similar to batteries than to capacitors. Electrode materials that participate in redox reactions mediate electron transport, a phenomenon known as pseudocapacitance. Pseudocapacitance appears at the electrode interfaces, where Faradaic reactions take place. These reactions include energy transfers between the two layers and are similar to battery charging and discharging operations. But the capacitance is increased because of a certain relationship, which may be defined as the amount of energy absorbed (Δq) in proportion to the potential change (ΔV). Redox reactions

(resulting from the bonds in the compounds) appear during the charging and discharging phases, allowing the electrolyte and electrode to exchange energy. Interestingly, energy is expressed through the energy inherent in molecule bonds rather than being trapped within a "dielectric" layer. One significant disadvantage of these systems is their underlying theory: unlike electrostatic storage, the electrodes in these systems experience stress and deterioration more quickly during cycles of charge and discharge.

These systems employ electrodes constructed from conductive polymers or transition metal oxides that demonstrate substantial pseudocapacitance. They accumulate electrical energy via charge transfer mechanisms occurring between the electrode and the electrolyte, frequently entailing oxidation-reduction reactions.

1.3.3.3 Hybrid Capacitors:

Hybrid supercapacitors are the latest version of supercapacitors and the most used in the field today. Representing the best version developed, this state-of-the-art version fuses the best features of the two preceding models: EDLCs and pseudo-supercapacitors. The hybrid supercapacitor thus gains the most by being able to dispense large currents and increased volumetric as well as gravimetric energy densities. The high energy density in hybrid supercapacitors arises from Faradaic reactions at the negative electrode, which mostly comprises pseudocapacitive materials, while the positive electrode is usually made of activated carbon, thereby making it easy for electrostatic energy to be stored in the double layer that covers the surface of the electrode. High current discharge is made possible in hybrid supercapacitors by the electrostatic interaction between charge carriers and the positive electrode surface. Just like lithium-ion batteries, hybrid supercapacitors have both structures and functionalities. Presently, these hybrid supercapacitors are only subjected to laboratory trials and not present in the commercial domain. [11].
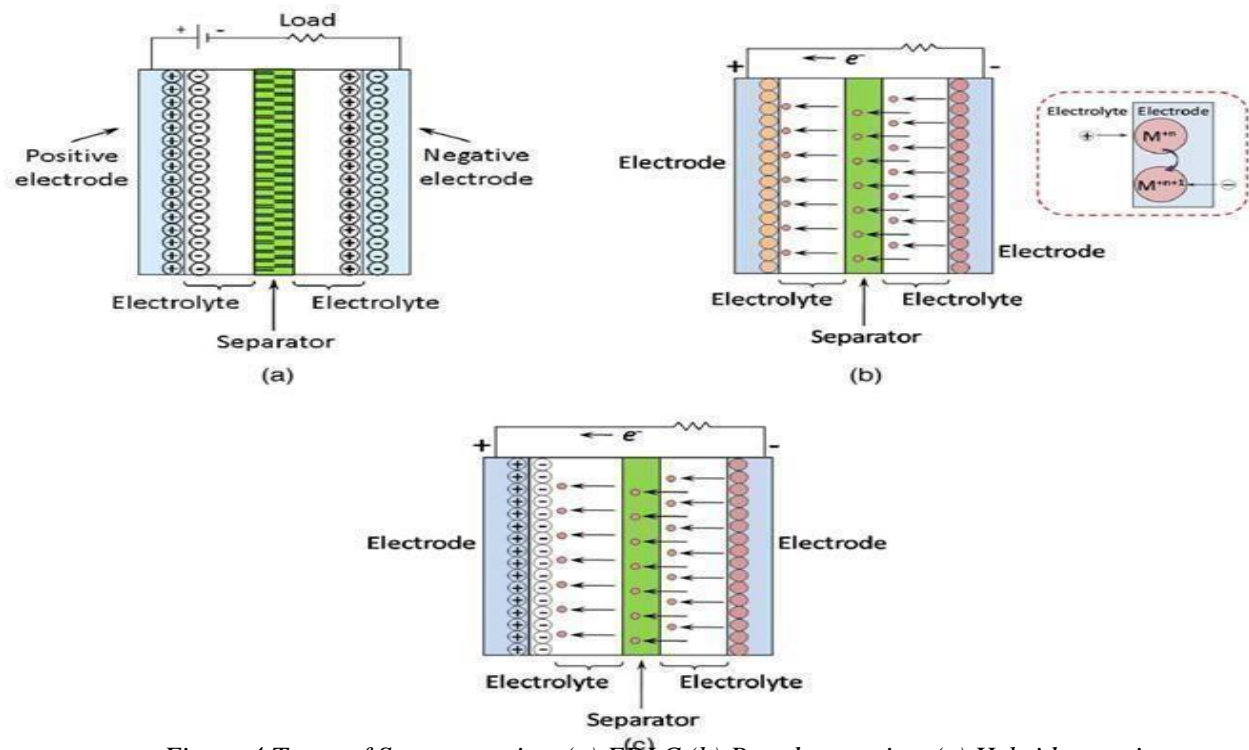
Figure 4 Types of Supercapacitor (a) EDLC (b) Pseudocapacitor (c) Hybrid capacitor

1.3.3 Differences Between Batteries and Supercapacitors

Key differences between batteries and SCs include their storage mechanisms, power capabilities, energy storage capacity, charging rates, and lifespan. For instance, batteries have kinetically limited charge rates, whereas SCs can charge as quickly as they discharge. SCs boast an exceptionally long cycle life (ranging from 30,000 to 1 million hours) compared to batteries (around 500 hours), alongside significantly shorter recharge times (SCs: 1–10 seconds vs. batteries: 10–60 minutes) [12].
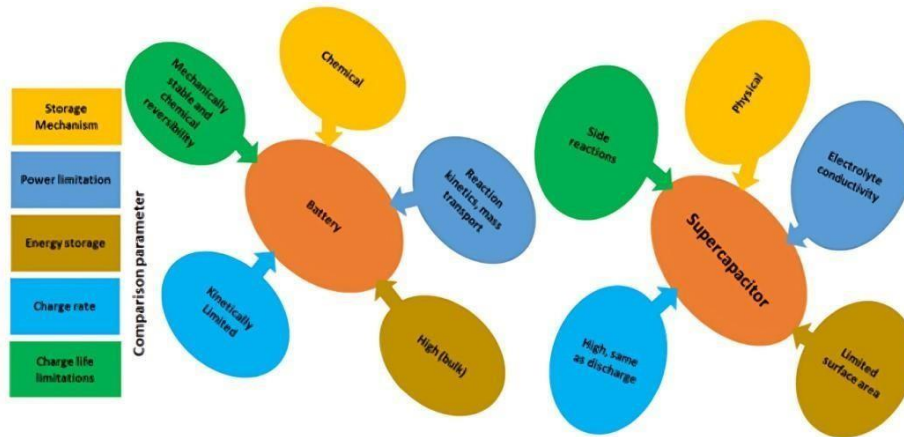
Figure 5 Comparison between batteries and SCs through different operational parameters

The performance of supercapacitors (SCs) greatly depends on the choice and design of electrode materials. Effective electrodes for SCs are characterized by:

- Thermal endurance,

- High specific surface area (SSA),

- Resistance to corrosion,

- Excellent electrical conductivity,

- Chemical stability,

- Optimal surface compatibility with electrolytes.

Furthermore, these materials should be cost-effective and environmentally friendly, with a strong ability to facilitate faradaic charge transfer, thus boosting capacitive efficiency.

The specific capacitance is influenced not only by the surface area but also by other critical factors such as the distribution and dimensions of pores, along with their shapes and accessibility to the electrolyte.

1.4 Types of electrode material:

Electrode materials fall into three primary categories:

- Carbon-based materials,

- Transition Metal Oxides (TMOs),

- Conductive Polymers (CPs).

1.4.1 Carbon-based Materials:

The most favored carbonaceous materials for use in EDLCs are due to large surface areas, affordability, environmental friendliness, and simple manufacturing processes. The physicochemical properties of such materials are mainly influenced by the pore sizes, usually smaller than 1 nm. The main principle behind the charge storage process at carbon-based electrodes lies in the formation of a Helmholtz plane, composed of both weakly and totally dissociated ions, at the electrode-electrolyte interface. Additionally, solvated ions strongly attracted to the electrode may replicate to an extended Gouy-Chapman diffuse layer under the control of thermal kinetics and solvated ions, with the resulting increase in the outer Helmholtz

layer. This voltage difference of these interior and exterior layers, or zeta, is then measured quantitatively to express the charge retention capacity of an EDLC.

1.4.1.1 MXenes:

 Introduced by Gogotsi and Barsoum in 2011, MXenes have captivated the research community with their remarkable attributes. MXenes, which are transition metal carbides, and nitrides, as well as carbonitrides, are produced by etching MAX Phase by removing the 'A' layers. Here, transition metal is represented by M, group 13 or 14 element is present in the center represented as A, and carbon or nitrogen is present at the end represented by X. Unlike other layered materials where Van Der Waals forces hold the structure like in graphene or TMDs, MAX phases feature strong covalent, metallic, or ionic bonds. The selective etching process removes the 'A' layers without disturbing the M-X bonds, resulting in the 2D MXene structure.

MXenes have been used due to their 2D structure and distinguished properties. They serve as catalysts in oxygen reduction and evolution reactions (ORR and OER), as well as CO oxidation reactions. Additionally, MXenes are utilized in sensor technology, including electrochemical biosensors and gas sensors, and for detecting macromolecules and cells. In energy storage, MXenes show promise as electrodes, where their surface functional groups and layered structure contribute to superior supercapacitive performance. Adjusting the interlayer distances in MXenes can further enhance their supercapacitive properties[13].

Three-dimensional structures offer a higher specific surface area than two-dimensional films, which are more prone to reaggregation, and are therefore the best means of utilising the unique features of MXenes. For example, three-dimensional MXenes with an internally connected porous matrix exhibit superior electromagnetic wave absorption performance compared to their two-dimensional MXene film counterparts in terms of electromagnetic interference shielding. Target reactant-MXene surface contact is important for applications including energy storage, water purification, and catalysis. In this case, a higher functional accessibility

of the MXene surfaces is enabled by the expansive configuration of three-dimensional MXenes. Furthermore, three-dimensional MXenes have excellent mechanical properties due to their sturdy lamellar architecture, which makes them useful for sensing applications. The shift from two-dimensional MXenes to three-dimensional structures appears to be a powerful remedy for the problems arising from the latter's flat configuration. One benefit of three-dimensional MXene designs is that: (1) MXene's extensive surface area is retained in three-dimensional structures due to the efficient suppression of nanosheet restacking.

Consequently, the electrolyte has access to an abundant proliferation of electrochemically active locations, expanding the range of electrochemical interactions; (2) The complex channels found in the three-dimensional MXene structures provide a pathway for quick electrolyte penetration; additionally, because of their excellent electrical conductivity, these structures function as excellent active electrodes and current distributors, enabling the quick passage of charge carriers through the porous matrix; (3) Functional group enhances the potential to engineer three-dimensional MXene structures with a variety of functionalities; (4) in real-world applications, the three-dimensional conductive configurations ensure effective charge movement across the entire volume of dense electrodes, a feature that greatly contributes to the maximisation of active material utilisation, regardless of electrode thickness or the mass of active material involved. Thus, it should come as no surprise that three-dimensional designs offer significant advantages for applications involving high-performance energy storage and conversion.

MXenes can be commonly synthesized by aqueous chemical exfoliation of atomic strata from a multilayered MAX phase. This process is based on the finding that intralayer cohesion is far more robust than interlayer adhesion inside a MAX phase. M-A bonds are first broken when the MAX phase is submerged in an acidic solution. The main etchant was found to be hydrofluoric acid (HF), which could be used directly or by reacting with a fluoride salt to generate HF in situ. The interaction of outer layer metals with acids results in surface terminations. These priceless materials combine the best qualities of metals and ceramics. They are similar to metals in that they allow heat and electricity to flow through them, but they are

also durable, thermally stable, fragile, and of excellent stiffness. There is a significant difference between M-A bond of MXenes and other stratified compounds, such graphite, where the former shows stronger van der Waals forces and the latter, metallic contacts. As a result, it is difficult to separate MXenes, which makes it more difficult to integrate additional functional elements effectively and reduces the amount of surface active sites available. Because of the relatively strong interlayer connections, mechanical separation or ultrasonication cannot easily achieve the delamination.
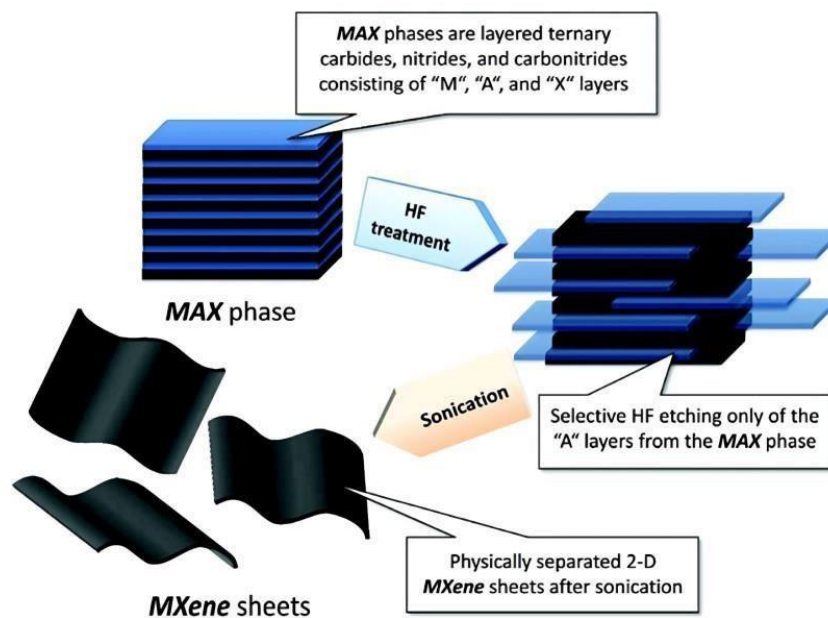
Figure 6 Etching of MXene from MAX phase

1.4.2 Oxides of Transition Metals (TMOs):

Compounds based on transition metals (TMs) are widely recognized for their redox capabilities, making them popular choices for supercapacitor (SC) electrodes, particularly in hybrid supercapacitors (HSCs), in the form of oxides and hydroxides. Commonly utilized TMs in TMOs and transition metal hydroxides (TM(OH)s) include elements like Ni, Fe, Co, Ti, Mo,

V, and Nb. TMOs present a viable alternative to carbon materials for SC electrodes due to their superior specific capacitance, reduced resistance, and enhanced conductivity.

Metal oxides play a pivotal role in the realms of energy conversion, storage, and catalysis across various electrochemical systems. These materials exhibit diverse properties, making them suitable for a range of electrochemical devices. Specifically, ruthenium oxide and iridium oxide are employed in oxygen evolution reactions (OER) for water splitting, a critical process in generating clean energy. Additionally, metal oxides like manganese dioxide and cobalt oxide, used as cathode materials in metal-air batteries, facilitate efficient oxygen reduction reactions (ORR). Cobalt, iron, nickel, and manganese oxides are also integral to energy storage technologies, with their performance optimized through particle size adjustment, morphology control, doping, and the creation of heterostructures [14].

1.4.3 Conductive Polymer-Based Materials:

Conductive Polymers (CPs) have gained attention as another class of pseudocapacitive electrode materials due to their:

- Notably high capacitance,

- Elevated energy density,

- Tunable redox properties via chemical modifications,

- Enhanced conductivity when doped,

- Wide operational voltage windows,

- Straightforward synthesis,

- Minimal environmental impact,

- Affordability.

CPs are capable of storing charge throughout their bulk without undergoing structural transformations like phase shifts during charging and discharging. This attribute allows CPs to achieve higher capacitance values, benefiting from extensive surface areas and redox storage capacities.

CPs are characterized by their robust redox activity and electron affinity. The physical properties of these polymers are largely influenced by their molecular weight. The chemical properties, predominantly determined by the polymer chains, exhibit stability in aqueous environments. CPs are typically synthesized through electrochemical polymerization by applying voltage or current across electrodes or by chemically oxidizing the monomer with oxidants [15].
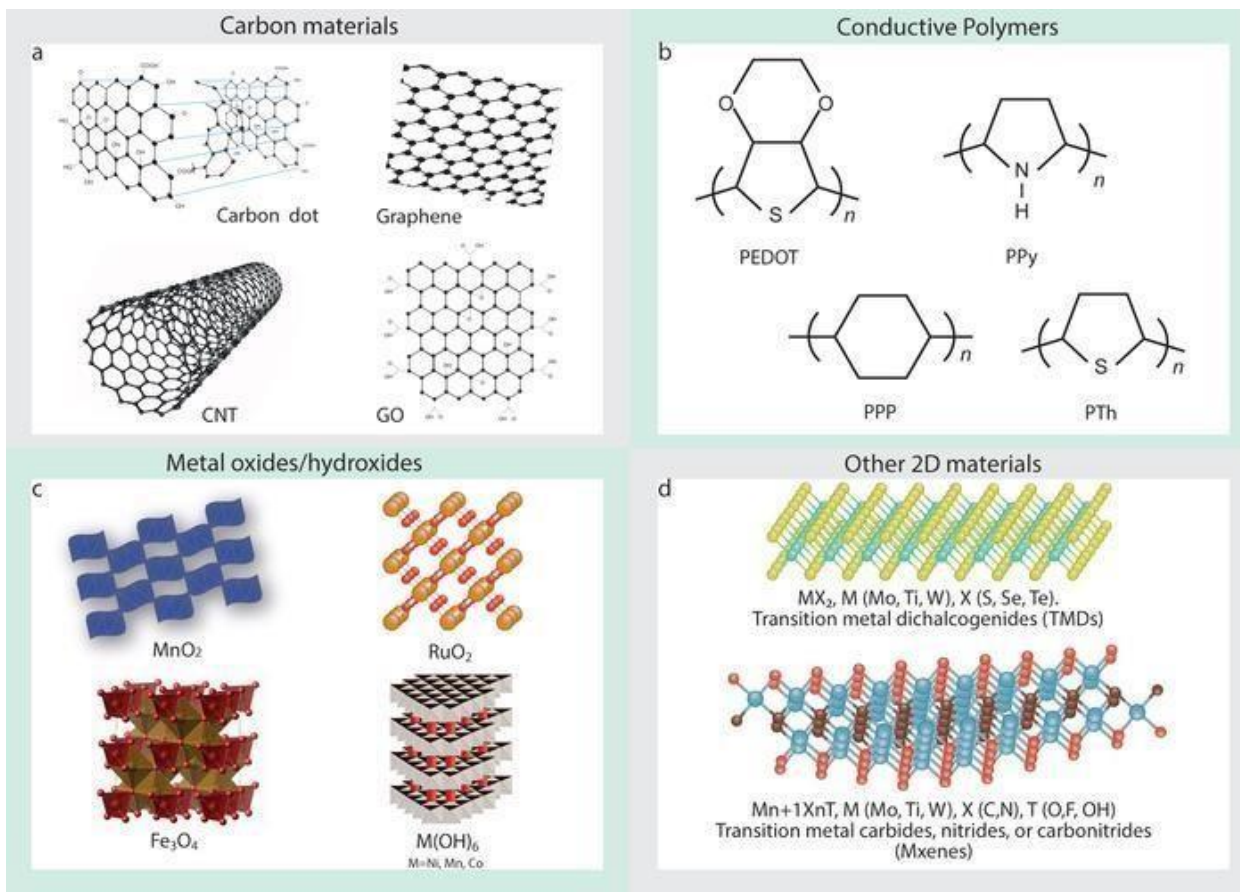
Figure 7 Different types of materials used for electrochemical energy storage

Chapter 2: Literature review

Numerous studies have been documented that explore these specific applications. Below is an overview of the materials developed and described in these studies for the purpose of enhancing supercapacitor and energy storage device performance.

Table 1 Literature review

SR.#	Material	Synthesis	Activity	Reference
1.	$CuFe_2O_4$–Fe_2O_3 composite	co-precipitation	638.24 Fg^{-1} supercapacitance at 10 mVs^{-1}	[16]
2.	$NiFe_2O_4$	Hydrothermal method	240.9 F/g supercapacitance at 1 A/g, Stability of 95% at 8 A/g	[17]

3.	CuO cauliflowers	Electrodeposition	179 F/g having 81% retention at 2000 cycles.	[18]
4.	Zn doped $MgFe_2O_4$ nanocrystals	sol–gel citrate method	highest specific capacitance of 484.6 Fg-1 at 1 mAcm-2 with 2 wt% Zn doped $MgFe_2O_4$	[19]
5.	2D/2D 1T-MoS_2/Ti_3C_2 MXene	magneto-hydrothermal processing	386.7 F g−1 at 1 Ag−1. Rettention of 98.6% after 10 000 cycles,	**[20]**
6.	Polypyrrole nanospheres/Ti_3C_2-MXene	in situ polymerizations	458 F g−1 at 2 mV s−1 in 1.0 M H2SO4 solution. Retention of 73.68% at 1A	**[21]**

			g−1 reaching 4000 cycles	
7.	Ti$_3$C$_2$-Mn$_3$O$_4$ Nanocomposite	solvothermal process	128 mAh/g at 1 A /g in a 6 M KOH. Retention of 77.7% after 2000 cycles at 10 A/g	**[22]**
8.	CoFe$_2$O$_4$ nanosheets	Hydrothermal method	503 F g−1 at 2A/g.	**[23]**
9.	Graphene@PANI	In-situ polymerization	480 F/g at 0.1 A/g	**[24]**
10.	CNT/V$_2$O$_5$ nanowire composite	one-pot hydrothermal process	663 C g− 1	**[25]**

2.1 Electrochemical Energy Production:

1. Rashid Khan and colleagues reported the synthesis of $CuFe_2O_4$–Fe_2O_3 composite material for efficient and highly stable supercapacitor electrode by using eco-friendly low-temperature co-precipitation method. The $CuFe_2O_4$–Fe_2O_3 composite demonstrated the highest specific capacitance of 638.24 F g−1 and excellent stability up to 2000 charge/discharge cycles. The achieved capacitance value is 16 times higher than that of pure $CuFe_2O_4$. The results revealed the extraordinary performance of $CuFe_2O_4$-Fe_2O_3 composite as supercapacitor electrode with excellent retention in comparison to $CuFe_2O_4$. The enhanced electrochemical activity of $CuFe_2O_4$–Fe_2O_3 composite is attributed to the synergistic effect which is responsible for redox coupling between Cu^{2+} and Fe^{3+} that has never been achieved by single component before.

2. Gao and colleagues developed $NiFe_2O_4$ with varying shapes using a straightforward hydrothermal technique. They discovered that employing urea as a precipitating agent (NFO-U) resulted in nanosheets, whereas using sodium acetate (NFO-C) led to a nanoparticle configuration. Both variations of NFO exhibited strong crystallinity. NFO-U demonstrated a specific capacitance of 240.9 F/g at a current density of 1 A/g, and its cycle life was impressive, with specific capacitance increasing to 128% after 2000 cycles. The nanosheet form of NFO showed superior specific capacitance compared to the spherical form, maintaining 95% of its capacitance at a current density of 8 A/g.

3. Deepak P. Dubal and colleagues synthesized and examined unique cauliflower-shaped CuO. They were synthesized through potentiodynamic mode from an alkaline aqueous solution. XRD confirmed the monoclinic structure of the CuO cauliflowers. SEM revealed a uniform distribution of CuO cauliflowers across the substrate, having 49 m²/g surface area. Electrochemical evaluations indicated that the CuO cauliflower achieved a high specific capacitance of 179 F/g in 1 M Na_2SO_4 electrolyte, with 81% capacity retention after 2000

cycles, attributing to efficient electrolyte penetration and enhanced Faradaic reactions due to its porous structure.

4. Santosh J. Uke and colleagues used a sol-gel citrate method to create $MgFe_2O_4$ nanocrystals doped with varying concentrations of zinc (Zn). These electrodes were applied to stainless steel substrates, using grade 304 stainless steel as the current collector. The material showcased significant specific capacitance, energy density, and cyclic stability as a supercapacitor electrode. Electrochemical assessments, including cyclic voltammetry, galvanostatic charge-discharge, and impedance spectroscopy, were performed, revealing a peak specific capacitance of 484.6 F/g and an energy density of 10.8 Wh/kg at a current density of 1 mA/cm² for the 2 wt% Zn-doped $MgFe_2O_4$, indicating superior performance in supercapacitor applications due to its structural and surface properties.

5. Xin Wang and colleagues synthesized a 2D/2D heterostructure combining $1T-MoS_2$ and Ti_3C_2 MXene. MoS_2, a well-studied 2D transition metal dichalcogenide, exhibits both a stable 2H phase and a metastable 1T phase, with the latter being highly effective for supercapacitor electrodes. The $1T-MoS_2$, synthesized via a template-solvothermal route, showed a specific capacitance of approximately 329 F/g in 1 M H_2SO_4 electrolyte. Ti_3C_2 MXene was obtained by etching Ti_3AlC_2 powders in hydrofluoric acid. The combination of $1T-MoS_2$ nanosheets with Ti_3C_2 MXene in a heterostructure resulted in a specific capacitance of 386.7 F/g at 1 A/g, with the synergistic interaction between the two materials enhancing the electrochemical performance.

6. Dan Wei and colleagues developed a strategy to create a polypyrrole nanospheres/Ti_3C_2-MXene (PPy/Ti_3C_2) heterostructure nanocomposite for advanced supercapacitor electrodes.

PPy nanospheres, with an average diameter of about 75 nm, were anchored on ultrathin Ti_3C_2 nanosheets through in situ polymerization. Electrochemical testing in a 1.0 M H_2SO_4 solution showed that the PPy/Ti_3C_2 nanocomposite exhibited a specific capacitance of 458 F/g, significantly exceeding that of pristine Ti_3C_2. The optimized PPy/Ti_3C_2 nanocomposite demonstrated good cycling stability, retaining 73.68% of its initial capacitance after 4000 cycles.

7. Kabir O. Oyedotun and colleagues introduced a simple two-step synthesis route to develop cost-effective, high-performance Ti_3C_2-Mn_3O_4 nanocomposite electrode materials through a solvothermal process. This method allowed precise control over the size, shape, and crystallinity of the metal oxide nanostructures by integrating Mn_3O_4 into the Ti_3C_2 layers to leverage the surface functionalities of the MXene sheets. Characterization confirmed a layered nanosheet structure with metal oxide nanoparticles integrated into the interlayer spaces. Electrochemical testing showed a maximum specific capacity of 128 mAh/g at a specific current of 1 A/g in a 6 M KOH aqueous electrolyte, with a capacity retention of 77.7% after over 2000 cycles.

8. Hongyan Gao and collaborators skillfully synthesized mesoporous $CoFe_2O_4$ employing a facile hydrothermal method on Ni foam, subsequently subjected to an annealing procedure. These $CoFe_2O_4$ nanosheets were deployed as electrodes in supercapacitors, exhibiting an exceptional 503 F/g specific capacitance at 2 A/g with 78.5% (395 F/g) capacitance retention at 20 A/g. An avant-garde aqueous asymmetric supercapacitor (ASC) was engineered utilizing $CoFe_2O_4$ nanosheets as the anodic material and activated carbon (AC) as the cathodic material, denoting its inaugural construction. This innovatively configured ASC manifested a specific capacitance of 73.12 F/g at a current density of 1.2 A/g within a 1.5V operational voltage, achieving a notable energy density of 22.85 Wh/kg coupled with outstanding long-term cycling fidelity

(98% retention following 5000 cycles). The electrode composed of $CoFe_2O_4$ nanosheets distinguishes itself through its elevated capacitance, distinguished cycling robustness, economic viability, and uncomplicated fabrication methodology, positioning it as an exemplary contender for supercapacitor implementations.

9. Graphene@polyaniline (PANI) nanofiber composites can be formed by in-situ polymerization. Following the polymerization, the graphene oxide/PANI composites underwent reduction to graphene via hydrazine, with subsequent reoxidation and reprotonation of the reduced PANI, resulting in graphene/PANI nanocomposites. Characterization techniques such as X-ray diffraction (XRD), solid-state 13C NMR, FT-IR, scanning and transmission electron microscopy (SEM and TEM), thermogravimetric analysis (TGA), and X-ray photoelectron spectroscopy (XPS) were employed to analyze the morphology, composition, and electronic structure of the composites along with pure polyaniline fibers (PANI-F), graphene oxide (GO), and graphene (GR). The analyses revealed that the graphene and PANI nanofibers formed a uniform nanocomposite, with PANI fibers either adhered to the graphene surface or intercalated between graphene layers. This uniform structure, coupled with high conductivity, contributed to a high specific capacitance and robust cycling stability as supercapacitor electrodes, achieving a specific capacitance of up to 480 F/g at a current density of 0.1 A/g in a PANI-doped graphene composite. The findings indicate that doping chemically modified graphene with PANI or incorporating graphene/graphene oxide into bulk PANI can significantly enhance specific capacitance and cycling stability.

10. A CNT/V_2O_5 nanocomposite was synthesized via a one-step hydrothermal method, employing aqueous vanadium oxide precursors and hydrophilic CNTs that had been pretreated. The electrolyte used was a 1 M $LiClO_4$ solution in propylene carbonate (PC), with lithium foils serving as both counter and reference electrodes. To assess the charge storage capacity, electrodes were initially subjected to slow charge and discharge cycles. At a 2000 s charge/discharge interval, the CNT electrode delivered a capacity of 86 C/g between 1.8 and 4.0 V. The nanowire electrode, charged/discharged over 4 hours (C/4 rate), exhibited a total charge storage of 792 C/g, equivalent to a specific capacity of 220 mAh/g – a value on par with

crystalline V_2O_5 synthesized at higher temperatures. Given that the composite included 18 wt% CNTs, the anticipated capacity of the nanocomposite electrode was 663 C/g, based on the additive capacities of the individual components. This was confirmed by galvanostatic testing, which showed the nanocomposite electrode achieved a capacity of 650 C/g, indicating that each component independently contributes to the overall charge storage at slow charging and discharging rates.

Chapter 3: Experimental section

3.1 Materials:

Titanium Aluminium Carbide (Ti_3AlC_2) MAX phase, Hydroflouric acid HF, Copper (II) Nitrate Hexahydrate $Cu(NO_3)_2 \cdot 6H_2O$, Iron (iii) Nitrate Hexahydrate $Fe(NO_3)_3 \cdot 6H_2O$, distilled water, Ethanol, Sodium Hydroxide NaOH, Hydrochloric acid HCl, Potassium Hydroxide KOH were obtained from sigma Scientific Pvt (ltd). These chemicals are of analytical grade.

3.2 Experimental:

Methods used to synthesize different materials for this research are explained in this section.

3.2.1 Synthesis of $Ti_3C_2T_X$:

In the fabrication process of Ti3C2, a quantity of ten grams of Ti_3AlC_2 was submerged into 100 ml of 49% hydrofluoric acid (HF) solution. This mixture underwent agitation for 1 minute, subsequently maintained at a temperature of 60°C for a duration of 24 hours. Following this period, the specimen underwent a rinsing process with deionized water, and the MXene powder was efficiently separated from the supernatant through centrifugation. The separation process was conducted at a velocity of 5000 revolutions per minute (rpm) with deionized water until the pH value approached approximately 7, followed by a dual cleansing with ethanol. Subsequently, the samples were subjected to a drying process within a vacuum oven at a temperature of 80°C over a span of 24 hours. The resultant product was then meticulously pulverized and prepared for subsequent analytical procedures [26]. A schematic representation detailing the synthesis methodology of Ti_3C_2 is depicted in figure 7 below:
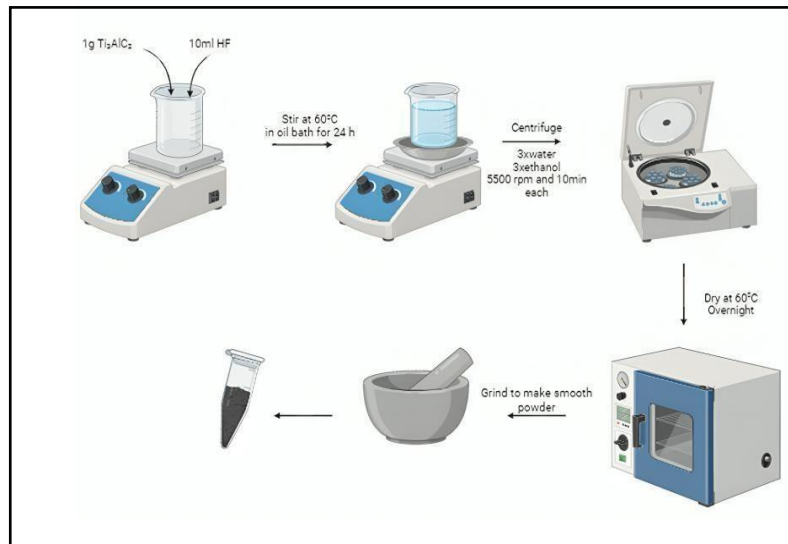
Figure 8 Diagramtic reperesentation of etching of MXene

3.2.2 Synthesis of CuFe2O4:

Utilizing this technique, we solubilized 0.05 mol of Cu(NO3)2·6H2O and 0.1 mol of Fe(NO3)3·6H2O into 150 ml of distilled water, subsequently introducing the solution into 100 ml of a 5 M NaOH solution, followed by a thermal treatment at 90 °C and a maturation period of 1.5 hours. The resultant sediment was subjected to filtration and rinsed with bi-distilled water, thereafter desiccated at 80 °C through the nocturnal hours. Conclusively, the synthesized powder was subjected to calcination at 630 °C for a duration of seven hours [27]. The schematic representation delineating the synthesis process of CuFe2O4 is exhibited in figure 8 below:
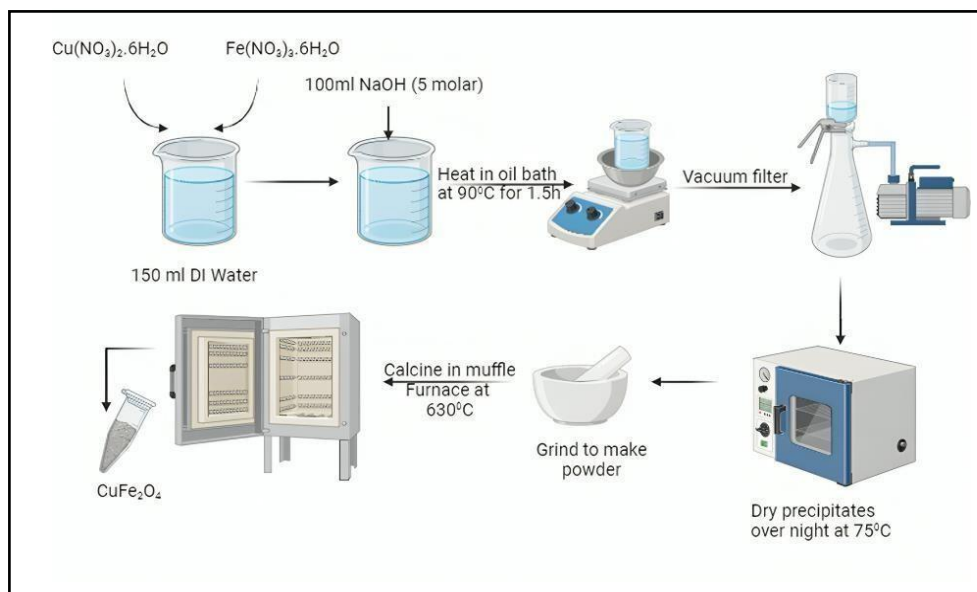
Figure 9 Graphical representation of synthesis of CuFe$_2$O$_4$

3.2.3 Synthesis of CuFe$_2$O$_4$/CuO-Ti$_3$C$_2$T$_X$ composite:

For synthesis of CuFe$_2$O$_4$-Ti$_3$C$_2$ composite, we dissolved 100mg Ti$_3$C$_2$ in 10 ml distilled water (sol1) and 50mg CuFe$_2$O$_4$ nanoparticles in 10 ml distilled water (sol2) and sonicated both these solutions for 30 minutes. After that we added sol 2 to sol 1 dropwise while sol1 was being continuously stirred. After mixing both solutions, it was kept for stirring for 30 minutes. The obtained precipitates were washed with distilled water for multiple times until supernatant became clear then dried at 80°C in vacuum oven for 12 hours. The diagram for the synthesis of CuFe$_3$O$_4$/CuO-Ti$_3$C$_2$T$_X$ composite is shown in figure 9 below:
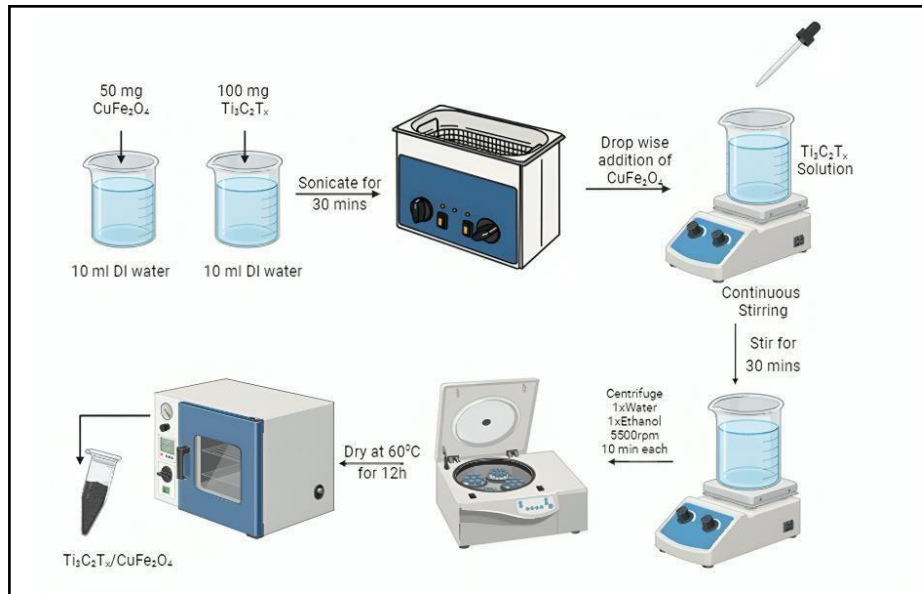
Figure 10 Graphical representation of synthesis of CuFe$_2$O$_4$/CuO-Ti$_3$C$_2$T$_X$ composite

Chapter 4: Results and discussions

This chapter includes the findings and discussions regarding the characterization and electrochemical studies (supercapacitance) of the materials including Ti_3C_2, $CuFe_2O_4/CuO$ and $CuFe_2O_4/CuO$- $Ti_3C_2T_X$

4.1 Characterization of materials:

Various characterization methods were applied to evaluate the materials. Crystallinity and phase composition of the materials were determined using X-ray diffraction (XRD) analysis with a Bourevestnik Dron 8 PXRD instrument. Scanning electron microscopy (SEM) was used to examine the surface morphology, while energy-dispersive X-ray spectroscopy (EDX) provided insights into the elemental composition. Additionally, the crystal structure, molecular vibrations, and chemical characteristics of the materials were analyzed using Raman spectroscopy with a Renishaw 2000 spectrometer.

4.1.1 X-ray Diffraction:

XRD of the materials were conducted to determine the crystal structure of all the catalysts in 2Θ range of 10-80.° The average crystalline size of all the materials were calculated by using the Scherrer equation which in given as:

$$D = \frac{k\,\lambda}{\beta \cos\theta}$$

Where D indicates the crystalline size of the material, λ is the wavelength, β is the FWHM and Θ is the peak position of the respective material.

The X-ray diffraction (XRD) analysis of pristine $Ti_3C_2T_X$ reveals a typical MXene phase, indicated by a peak at a 2θ angle of 8.2°, which corresponds to the (001) planes. The broad and intense nature of these peaks suggests that the material has a layered structure and a high level of crystallinity [28]. Since no additional peaks are observed, it implies that the material is a single phase, free from impurities or secondary phases. The broadening of the peaks indicates that the crystallite size is small, estimated to be about 10 nm, as calculated using the Scherrer equation.

For pristine $CuFe_2O_4/CuO$, the XRD pattern displays a well-defined spinel structure. The observed peaks at 2θ angles of 30.1°, 32.1°, 35.4°, 38.8°, 56.8°, and 62.5° correspond to the (022), (110), (131), (200), (151), and (044) planes, respectively. These peaks are sharp and intense, indicating a high degree of crystallinity and purity, with no extra peaks, which further confirms that the material is a single phase without impurities or secondary phases [29].

In the case of the $CuFe_2O_4/CuO-Ti_3C_2T_X$ composite material, the XRD pattern shows a combination of peaks that correspond to both $CuFe_2O_4$ and Ti_3C_2 phases. This confirms the successful synthesis of the composite material. The relative intensity of the peaks suggests that both phases are evenly distributed throughout the composite. Additionally, the absence of any unexpected or additional peaks indicates that the composite material is pure and free from secondary phases.
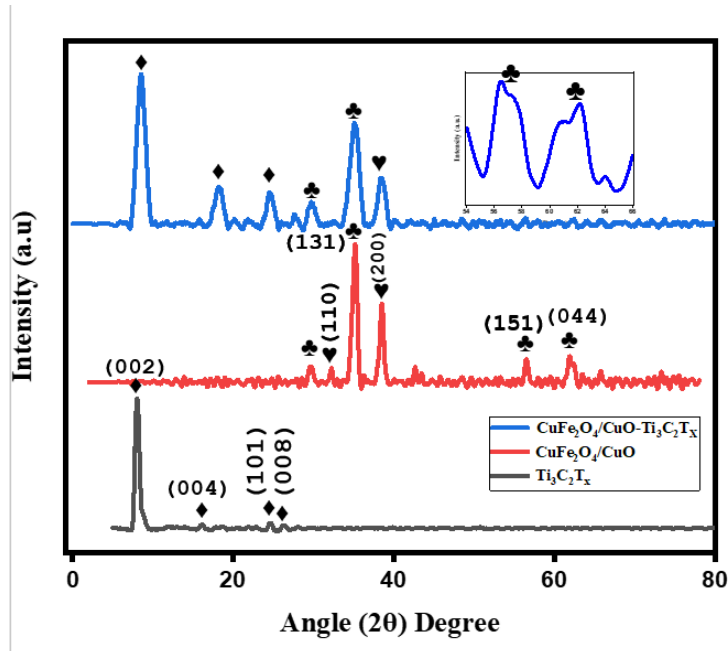
Figure 11 XRD of Ti₃C₂Tₓ, CuFe₂O₄/CuO, CuFe₂O₄/CuO-Ti₃C₂Tₓ

4.1.2 FTIR Spectroscopy:

Copper Ferrite (CuFe₂O₄/CuO) - showing two peaks at 424 cm-1 and 477 cm-1. Titanium Carbide (Ti₃C₂Tₓ) - showing four peaks at 597 cm-1, 532 cm-1, 487 cm-1 and 431 cm-1 . Composite material (CuFe₂O₄/CuO + Ti₃C₂Tₓ) - showing four peaks at 593 cm-1, 532 cm-1, 477 cm-1 and 424 cm-1 [30].

The peaks in the FTIR spectra represent vibrational modes of the chemical bonds present in the materials. In the composite material, you see a combination of peaks from both Copper Ferrite and Titanium Carbide. Slight shift in peak positions (e.g., 597 cm-1 to 593 cm-1) may indicate interactions or bonding between the two materials. The presence of all peaks from both materials in the composite suggests a physical mixture or dispersion of the two materials, rather than a chemical reaction or complete alloying.
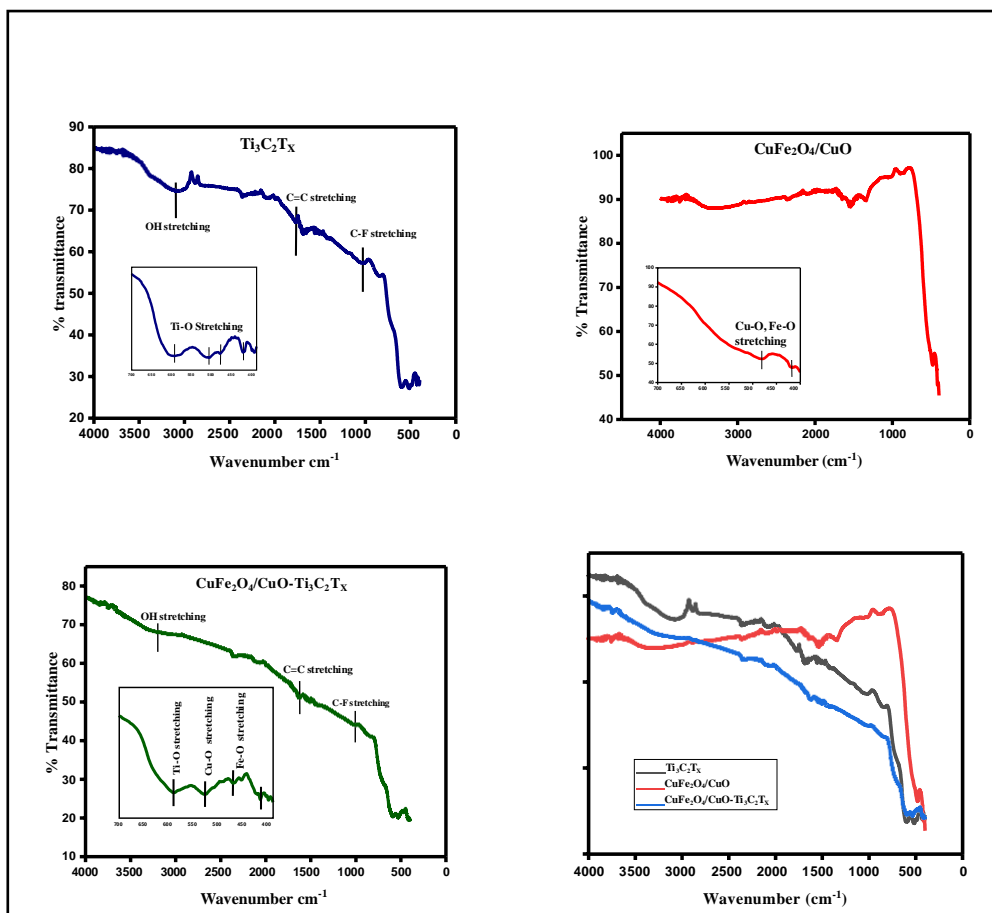
Figure 12 FTIR spectra of $Ti_3C_2T_X$, $CuFe_2O_4/CuO$ and $CuFe_2O_4/CuO-Ti_3C_2T_X$

4.1.3 Raman Spectroscopy:

The Raman spectrum of $Ti_3C_2T_X$ Mxene exhibits three prominent regions, indicative of the material's structure and composition. The spectrum is characterized by:

- Flake region (low-frequency range, approximately 100-400 cm^{-1}): This region corresponds to the vibrational modes of the $Ti_3C_2T_X$ Mxene flakes, associated with the in-plane and out-of-plane movements of the titanium and carbon atoms.

- Tx region (mid-frequency range, approximately 400-700 cm^{-1}): This region is attributed to the vibrational modes of the transition metal carbide (Tx) phase, resulting from the etching process of the MAX phase precursor. The Tx region is indicative of the material's defect structure and disorder.

- C region (high-frequency range, approximately 700-1200 cm^{-1}): This region corresponds to the vibrational modes of the carbon atoms in the $Ti_3C_2T_X$ Mxene structure, associated with the C-Ti bonding and the graphitic carbon layers [31].

The Raman spectrum of $CuFe_2O_4$ exhibits several prominent peaks, which can be attributed to the various vibrational modes of the material. The peak observed at approximately 670 cm-1 corresponds to the A1g mode, associated with the symmetric stretching of the oxygen atoms along the tetrahedral axes. The peaks at around 540 cm-1 and 450 cm-1 are attributed to the Eg and T2g modes, respectively, which arise from the bending vibrations of the oxygen atoms [32].

The observed Raman shifts and their corresponding assignments are consistent with the literature values for $CuFe_2O_4$, indicating the presence of a well-ordered spinel structure. The intensity and sharpness of the peaks suggest a high degree of crystallinity and purity of the material. These findings are in agreement with the X-ray diffraction analysis, which further confirms the formation of a single-phase $CuFe_2O_4$ material.

The presence of both $CuFe_2O_4$ and Ti_3C_2 peaks in the Raman spectrum confirms the successful synthesis of the composite material. The intensity and shape of the peaks suggest a uniform distribution of both phases within the composite. The $CuFe_2O_4$ peaks appear to be slightly broadened, indicating possible interactions between the two phases.
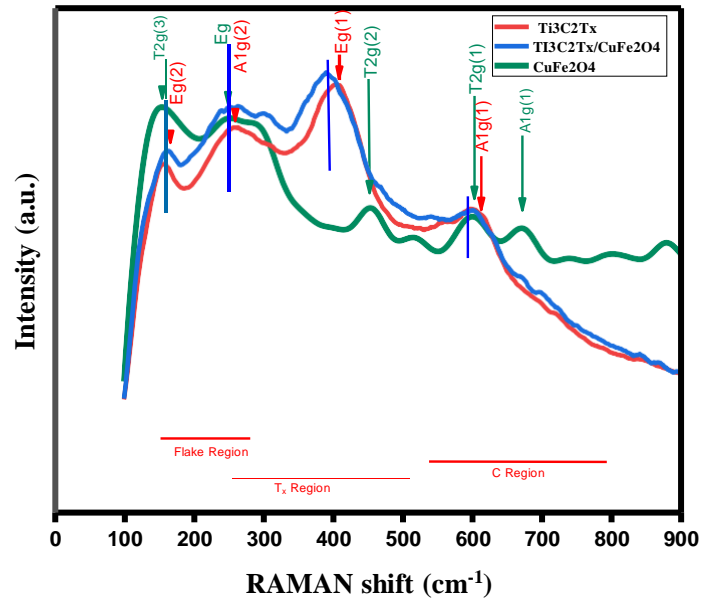
Figure 13 RAMAN spectra

4.1.4 SEM analysis:

To check the surface morphology, SEM (Scanning Electron Microscopy) analysis was performed. SEM images of $Ti_3C_2T_X$, $CuFe_2O_4/CuO$ and $CuFe_2O_4/CuO$- $Ti_3C_2T_X$ are shown below in figure. As seen in fig. 15, the MAX phase has an uneven and densely packed surface structure. Following the etching procedure, MXene developed a structural shape like an accordion. The parallel-oriented etched layers of Al are shown in Fig. 3b. Copper ferrite nanoscale entities were intercalated between the MXene layers. Cu+2 and Fe+2 ions make up copper ferrite, whilst a range of charged functional groups decorate MXene surfaces. Ferrite particles are pulled into the interstices by electrostatic forces upon the exfoliation of MXene sheets, increasing the c-lattice size.
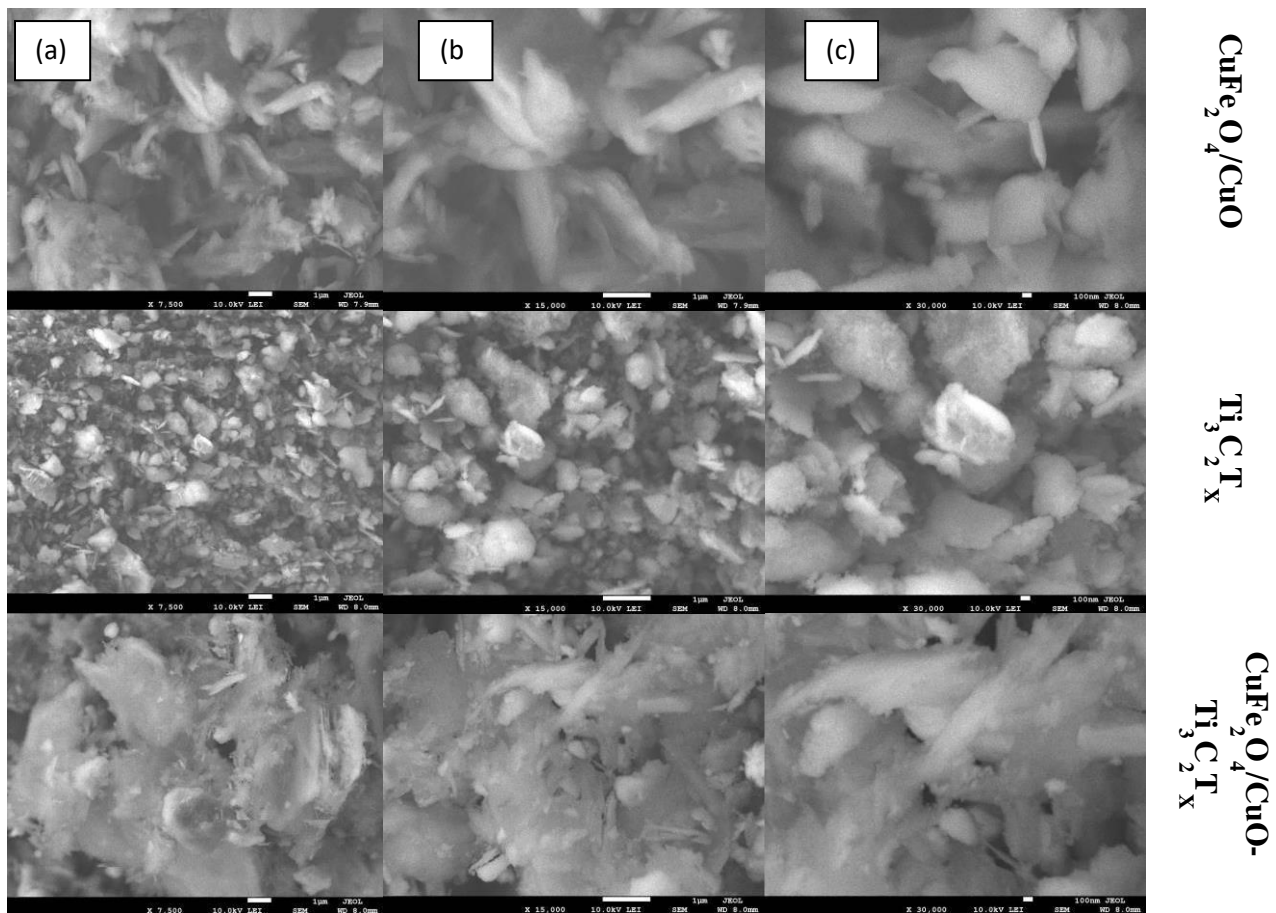
Figure 14 SEM images of Ti$_3$C$_2$T$_X$, CuFe$_2$O$_4$/CuO,CuFe$_2$O$_4$/CuO-Ti$_3$C$_2$T$_X$ (a) x 7500 (b) 15000 (c) 30000

4.2 Electrochemical measurements:

The EC measurements were done on Potentiation/Galvanostatic/ZRA (Gamrey Instrument) by utilizing the three electrode system by using a wire made of Platinum as a counter electrode along with reference electrode of Ag/AgCl. Working electrode was designed by depositing the material ink on Ni foam by drop cast method. For this purpose, Ni foam (2 cm X 1 cm) was first washed with 6 M HCl by sonicating it for 15 mints. Then the Ni foam was sonicated in DI water and ethanol for 15 minutes each. The slurry of material was prepared by taking 1 mg of product in 50 µl ethanol in an eppendorf and Nafion was used as binder and then sonicated it for 30 minutes. The prepared slurry was then deposited uniformly on the $1cm^2$ area of the Ni foam.
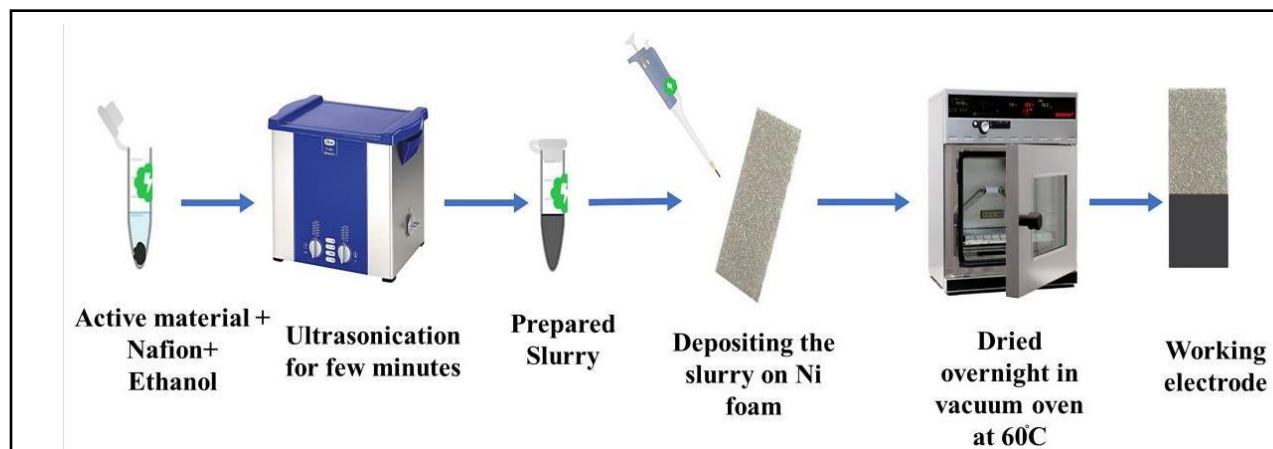
Figure 15 Graphical representation of fabrication of working electrode

The electrochemical measurements that were carried out for Ti_3C_2, $CuFe_2O_4$ and $CuFe_2O_4/CuO-Ti_3C_2T_X$ includes the GCD, CV, ECSA and EIS. CV was conducted to activate the material by running 50 cycles at range of 0-0.46 V vs Ag/AgCl at 100 mV/s SR. CV cycles were also performed at different scan rate of 5, 10, 20, 50, 75, and 100 mV s^{-1} at the same

potential range to determine the activity of the materials. ECSA was also calculated by running CV in the non-faradic region of 0.1-0.2 V at different scan rates. GCD at current densities of 1, 2, 4, 6, 8, and 10 A g^{-1} was performed to determine the supercapacitance activity of the materials. Moreover, EIS was also carried out to determine the resistance towards the electric conductivity of the material. All test were performed in 2 M KOH by utilizing three electrode systems. The detail of the following techniques is given as:

4.2.1 Galvanostatic Charge-Discharge (GCD):

GCD analysis was carried out to determine the charge storage activities of the material. GCD was conducted at different CD of 1, 2, 4, 6, 8, and 10 A/g. Cs is calculated from GCD analysis by the following formula:

$$Cs = \frac{I \ X \ dt}{m \ X \ dV}$$

The GCD profiles of $Ti_3C_2T_X$, $CuFe_2O_4/CuO$ and $CuFe_2O_4/CuO-Ti_3C_2T_X$ are shown in figure below. The figures indicate that $CuFe_2O_4/CuO-Ti_3C_2T_X$ composite exhibit greater charge/ discharge time and hence the greater specific capacitance. Greater surface area of the material is responsible for higher diffusion of electrolyte ions on the catalyst surface. This resulted in greater charge storage on the surface of material. Moreover, the higher porosity of material resulted in intercalation of the electrolyte ions to the material and hence increased charge storage.

The galvanostatic charge-discharge (GCD) profile of Ti_3C_2 showcases a near-perfect triangular shape, signaling exemplary capacitive characteristics. This profile highlights a swift charge-discharge action, achieving a specific capacitance of 1060 F/g. Notably, the discharge segment closely mirrors the charge phase, underscoring exceptional reversibility and Coulombic

efficiency. This behavior underscores the pseudocapacitive nature of Ti_3C_2, primarily driven by surface redox activities.

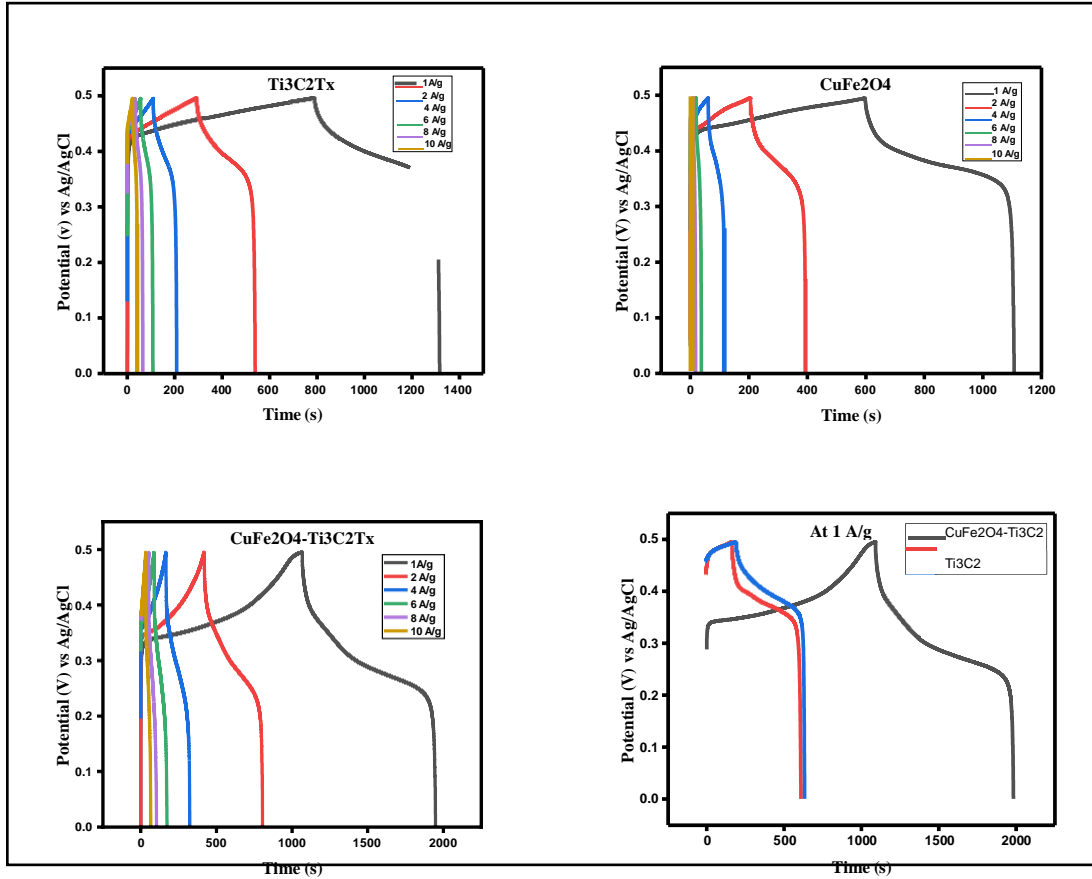*Figure 16 GCD profile of $Ti_3C_2T_X$, $CuFe_2O_4/CuO$, $CUFe_2O_4/CuO-Ti_3C_2T_X$*

In contrast, the GCD profile of $CuFe_2O_4$ assumes a quasi-triangular form, denoting a blend of capacitive and battery-like properties. This curve reveals a comparatively leisurely charge-discharge pace, with a specific capacitance reaching 1026 F/g. It suggests that the electrochemical behavior of $CuFe_2O_4$ stems from both surface redox activities and diffusion-driven processes.

The composite of $CuFe_2O_4$ and Ti_3C_2, however, demonstrates superior capacitive behavior in its GCD profile, with a remarkable specific capacitance of 1779 F/g—substantially surpassing the individual components. Compared to $CuFe_2O_4$ alone, this composite exhibits a quicker charge-discharge cycle, indicating enhanced electrochemical kinetics. The discharge phase

maintains excellent alignment with the charging phase, indicative of high reversibility and Coulombic efficiency. The GCD profile for this composite highlights a synergistic interaction between $CuFe_2O_4$ and Ti_3C_2, optimizing its pseudocapacitive behavior and elevating its energy storage capability.
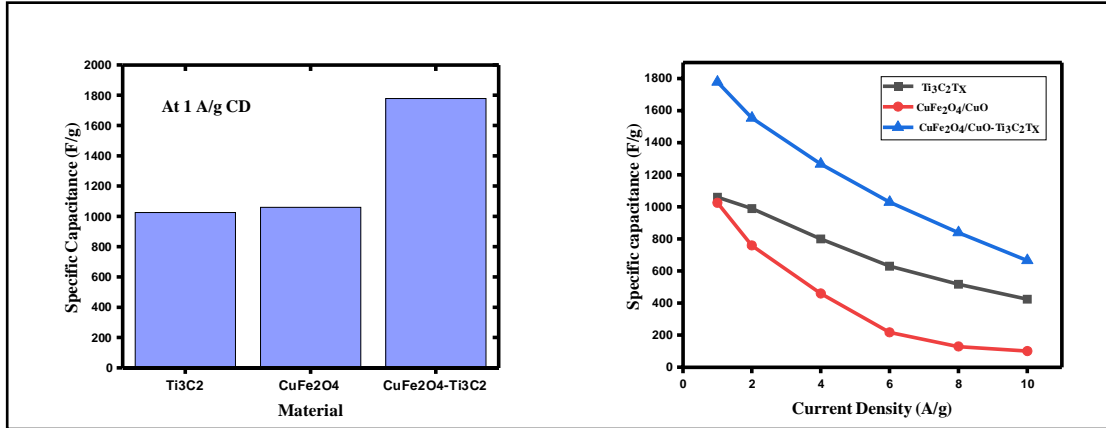

Figure 17. GCD comparison

It is found that Cs of $CuFe_2O_4/CuO-Ti_3C_2T_X$ is highest of all current densities. The comparison of all the materials GCD curves at 1 A/g and their Cs calculated from their GCD curves at various CD is shown in figure below. Moreover, the values of the Cs calculated for all electrodes are given in table below.

Current Density	Specific Capacitance (F/g)		
(A/g)	Ti_3C_2	$CuFe_2O_4$	$CuFe_2O_4/Ti_3C_2$
1	1060	1026	1779
2	989	759	1555
4	800	460	1268
6	630	218	1030
8	517	129	840
10	424	101	666

4.2.2 Cyclic voltammetry:

CV curves of $Ti_3C_2T_X$, $CuFe_2O_4/CuO$ and $CuFe_2O_4/CuO$-$Ti_3C_2T_X$ are shown in figure. CV is performed at scan rate of 5, 10, 20, 50, 75 and 100 mV/s between 0-0.46 V. The Cs of all materials has been calculated from CV profiles by using the following formula:

$$Cs = \frac{A}{2mk(dv)}$$

Where A is the area under the curve, m is the loading mass of the material, k is the scan rate and dv is the difference in potential window. The CV profiles indicated the pair of oxidation and reduction peaks, that is the indication of faradic reaction. It has been found that the CD rises with the increase in SR due to greater ion movements. This indicates the greater electrical conductivity of material and greater charge transfer.

The electrochemical performance of $Ti_3C_2T_X$, $CuFe_2O_4/CuO$, and $CuFe_2O_4/CuO$-$Ti_3C_2T_X$ composite exhibits distinct differences. $Ti_3C_2T_X$ shows a moderate specific capacitance of 135 F/g, indicating decent energy storage capability. In contrast, $CuFe_2O_4/CuO$ displays a relatively low specific capacitance of 95 F/g, suggesting limited energy storage capability. However, the $CuFe_2O_4/CuO$-$Ti_3C_2T_X$ composite demonstrates a significantly enhanced specific capacitance of 336 F/g, indicating an optimized pseudocapacitive behavior and improved energy storage capability. This synergistic effect suggests that the combination of $CuFe_2O_4/CuO$ and $Ti_3C_2T_X$ leads to an enhanced electrochemical performance, making the composite a more promising material for energy storage applications.
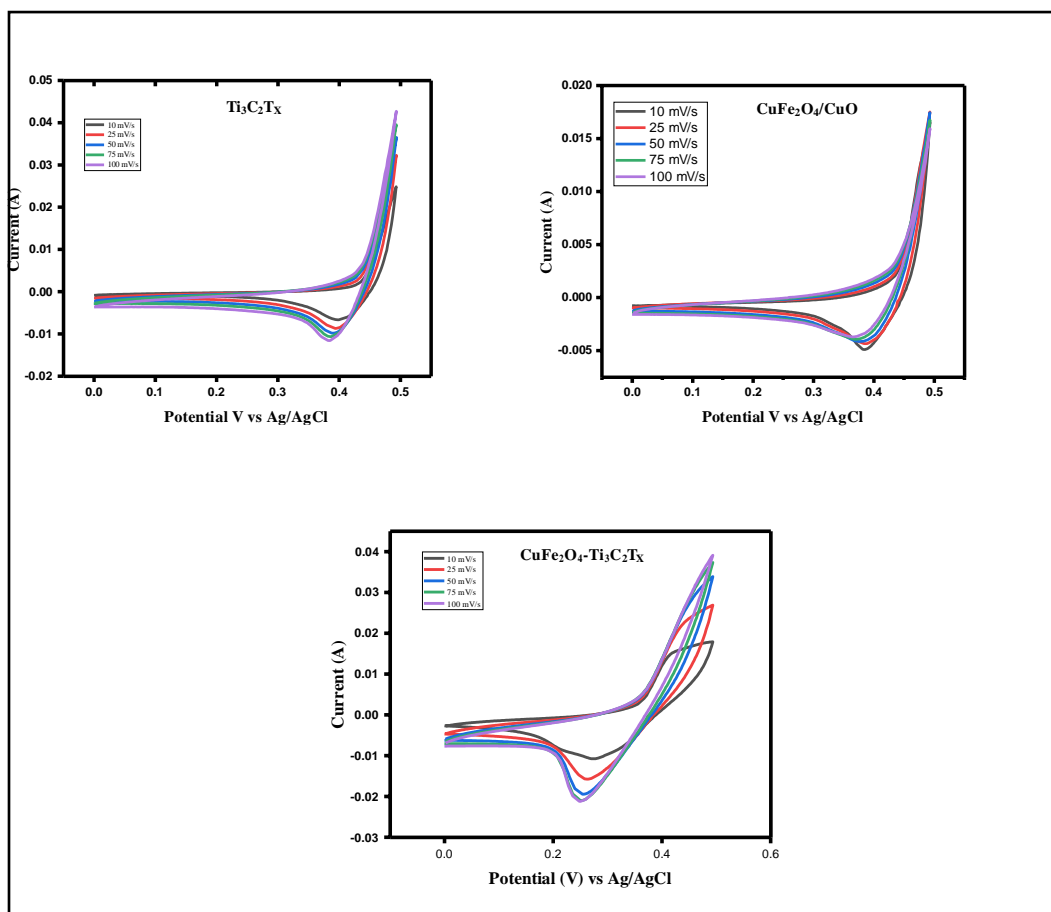
Figure 18 CV profile of Ti$_3$C$_2$T$_X$, CuFe$_2$O$_4$/CuO, CuFe$_2$O$_4$/CuO-Ti$_3$C$_2$T$_X$

Specific capacitance of all materials calculated from CV curves is given in table below. CuFe$_2$O$_4$/CuO-Ti$_3$C$_2$T$_X$ indicated the highest specific capacitance of all materials due to hybrid nature. It has been found that the Cs of material reduced with the increase in SR because fewer electrolyte ions diffuse on the electrode surface and electrode become less efficient for charge storage. The comparison or trend of specific capacitance for all the materials is shown in figure . CV profile of all materials at 25 mV/s SR is also compared and shown in figure.

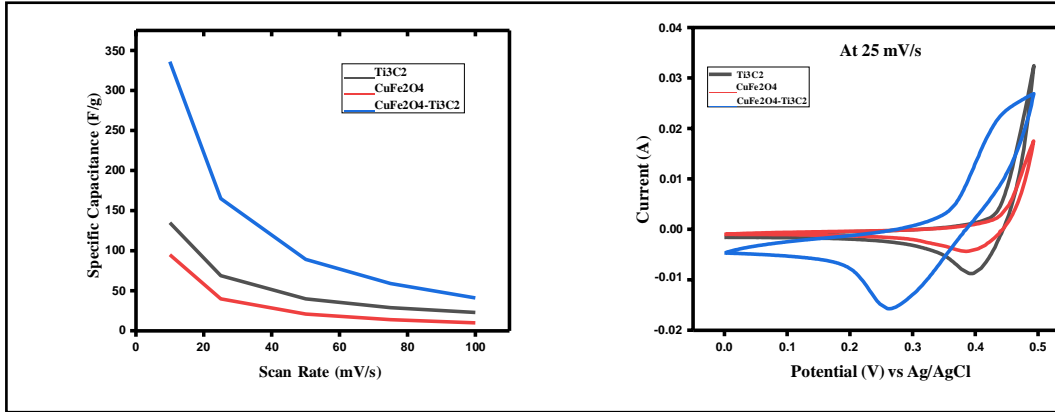| SAMPLE	Scan Rate (mV/s)					Specific capacitance
	10	25	50	75	100	
Ti$_3$C$_2$	135	69	40	29	23	
CuFe$_2$O$_4$	95	40	21	14	10	
CuFe$_2$O$_4$-Ti$_3$C$_2$	336	165	89	59	41	

Figure 19 CV comparison

4.2.3 Ragone plot:

The ED and PD of all the materials is calculated by specific capacitance from GCDs. The formulas for calculating the energy and power density of materials are given as:

$$Energy\ Density = \frac{1}{7.2} Cs * dv^2$$

$$Power\ Density = 3600 * \frac{E}{dt}$$

Ragone plot is drawn by plotting the Power density against energy density which is shown in figure. It can be seen from the graphs that the hybrid capacitors have high ED and power density at all current density values. This is because of the greater assessment of active sites.

The values of ED and PD at all current density are shown in table below
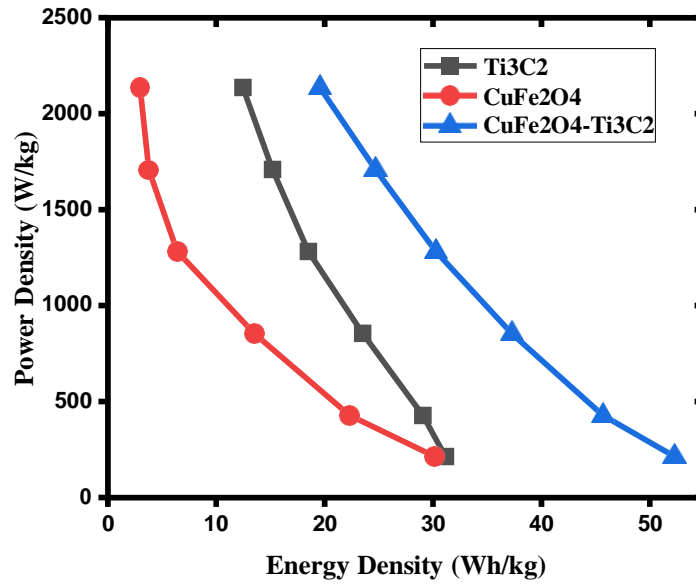
Figure 20 Ragone plot

Materials	1 A/g		2 A/g		4 A/g		6 A/g		8 A/g		10 A/g	
	ED	PD	ED	PD	ED	PD	ED	PD	ED	PD	ED	PD
Ti3C2	**31.15**	**213.6**	29.06	427	23.5	854	18.5	1281	15.1	1709	12	2136
CuFe2O4	**30**	**213.7**	22.3	427	13.5	853.8	6.4	1281	3.79	1706	2.96	2137
CuFe2O4-Ti3C2	**52.2**	**213.6**	45.6	427	37.26	854.5	30.27	1282	24.7	1709	19.6	2135

45

4.2.4 Capacitive retention of CuFe$_2$O$_4$/CuO-Ti$_3$C$_2$T$_x$ composite:

Stability of electrode for charge storage efficiency is determined by conducting GCD analysis. The ability of electrode to retain the specific capacitance after six thousand cycles was determined by conducting 6000 cycles at 0-0.46 V potential. The capacitive retention of material was found to be 97.3 % after these cycles. This indicates the high stability of the electrode material for charge storage devices. The coloumbic efficiency of the material was also determined by using the following formula:

$$Coloumbic\ Efficiency = \frac{Discharge\ Time}{Charge\ Time}$$

The graphs indicating the stability and coloumbic efficiency of material are shown in figure below.

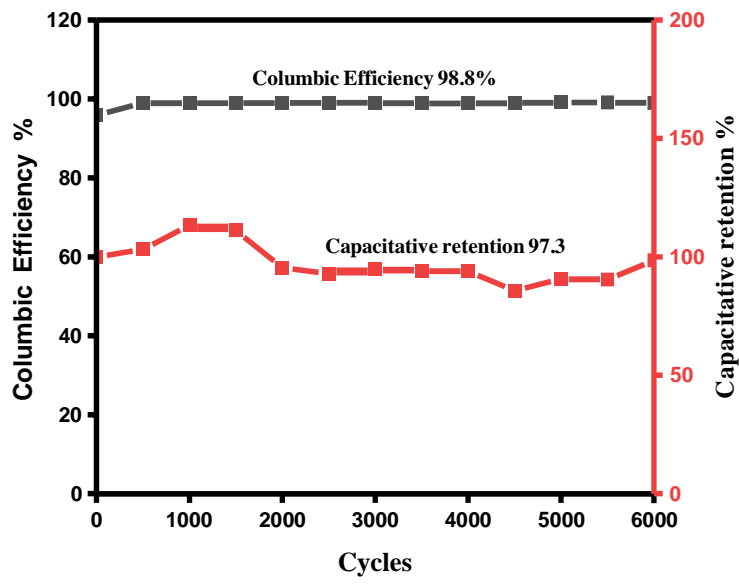*Figure 21 Columbic efficiency & Capacitative retention*

Chapter 5: CONCLUSION

The composite material $CuFe_2O_4/CuO$-$Ti_3C_2T_X$ was effectively created and applied as an electrode material. By integrating $CuFe_2O_4/CuO$ with $Ti_3C_2T_X$, the electrochemical properties of $Ti_3C_2T_X$ were significantly improved, addressing the limitations of both $CuFe_2O_4/CuO$ and $Ti_3C_2T_X$ when used separately. This combination material achieved an exceptional specific capacitance of 1779 F/g at a current density of 1 A/g and a potential of 0.46 V versus Ag/AgCl. Furthermore, it demonstrated a low resistance to charge transfer and a high surface area conducive to adsorption. The material maintained a Coulombic efficiency of 98.8% and a capacitive retention rate of 97.3%, indicating its stability and confirming its successful synthesis and application as an electrode material.

REFERENCES:

1. Raza, W., et al., *Recent advancements in supercapacitor technology.* Nano Energy, 2018. **52**: p. 441-473.

2. Singh, S., et al., *Hydrogen: A sustainable fuel for future of the transport sector.* Renewable and sustainable energy reviews, 2015. **51**: p. 623-633.

3. Goodenough, J.B., *Electrochemical energy storage in a sustainable modern society.* Energy & Environmental Science, 2014. **7**(1): p. 14-18.

4. Gonenc, H. and B. Scholtens, *Environmental and financial performance of fossil fuel firms: A closer inspection of their interaction.* Ecological Economics, 2017. **132**: p. 307-328.

5. Assembly, U.G., *Actions on climate change will define global legacy left for future generations.* UN Media Release, 2007. **24**.

6. Kalidindi, S.B. and B.R. Jagirdar, *Nanocatalysis and prospects of green chemistry.* ChemSusChem, 2012. **5**(1): p. 65-75.

7. Wang, H., Y. Yang, and L. Guo, *Nature-inspired electrochemical energy-storage materials and devices.* Advanced Energy Materials, 2017. **7**(5): p. 1601709.

8. Dunn, B., H. Kamath, and J.-M. Tarascon, *Electrical energy storage for the grid: a battery of choices.* Science, 2011. **334**(6058): p. 928-935.

9. Wachsman, E.D., C.A. Marlowe, and K.T. Lee, *Role of solid oxide fuel cells in a balanced energy strategy.* Energy & Environmental Science, 2012. **5**(2): p. 5498-5509.

10. Winter, M. and R.J. Brodd, *What are batteries, fuel cells, and supercapacitors?* Chemical reviews, 2004. **104**(10): p. 4245-4270.

11. Vangari, M., T. Pryor, and L. Jiang, *Supercapacitors: review of materials and fabrication methods.* Journal of energy engineering, 2013. **139**(2): p. 72-79.

12. Gröger, O., H.A. Gasteiger, and J.-P. Suchsland, *Erratum: Review—Electromobility: Batteries or Fuel Cells?[J. Electrochem. Soc., 162, A2605 (2015)].* Journal of the Electrochemical Society, 2016. **163**(7): p. X3.

13. Li, J., et al., *Achieving high pseudocapacitance of 2D titanium carbide (MXene) by cation intercalation and surface modification.* Advanced Energy Materials, 2017. **7**(15): p. 1602725.

14. Holze, R., *Metal oxide/conducting polymer hybrids for application in supercapacitors*, in *Metal oxides in supercapacitors*. 2017, Elsevier. p. 219-245.

15. Sasikumar, M., et al., *The effects of PVAc on surface morphological and electrochemical performance of P (VdF-HFP)-based blend solid polymer electrolytes for lithium ion-battery applications.* Ionics, 2019. **25**: p. 2171-2181.

16. Khan, R., et al., *Facile synthesis of CuFe2O4–Fe2O3 composite for high-performance supercapacitor electrode applications.* Materials Research Express, 2017. **4**(10): p. 105501.

17. Gao, X., et al., *Morphology-controllable preparation of NiFe2O4 as high performance electrode material for supercapacitor.* Electrochimica Acta, 2019. **296**: p. 181-189.

18.   Dubal, D.P., et al., *CuO cauliflowers for supercapacitor application: Novel potentiodynamic deposition.* Materials Research Bulletin, 2013. **48**(2): p. 923-928.

19.   Uke, S.J., et al., *Sol-gel citrate synthesized Zn doped MgFe2O4 nanocrystals: a promising supercapacitor electrode material.* Materials Science for Energy Technologies, 2020. **3**: p. 446-455.

20.   Wang, X., et al., *2D/2D 1T-MoS2/Ti3C2 MXene heterostructure with excellent supercapacitor performance.* Advanced Functional Materials, 2020. **30**(15): p. 0190302.

21.   Wei, D., et al., *A facile strategy of polypyrrole nanospheres grown on Ti3C2-MXene nanosheets as advanced supercapacitor electrodes.* Journal of Electroanalytical Chemistry, 2020. **877**: p. 114538.

22.   Oyedotun, K.O., et al., *Electrochemical performance of two-dimensional Ti3C2-Mn3O4 nanocomposites and carbonized iron cations for hybrid supercapacitor electrodes.* Electrochimica Acta, 2019. **301**: p. 487-499.

23.   Gao, H., J. Xiang, and Y. Cao, *Hierarchically porous CoFe2O4 nanosheets supported on Ni foam with excellent electrochemical properties for asymmetric supercapacitors.* Applied Surface Science, 2017. **413**: p. 351-359.

24.   Zhang, K., et al., *Graphene/polyaniline nanofiber composites as supercapacitor electrodes.* Chemistry of Materials, 2010. **22**(4): p. 1392-1401.

25.   Chen, Z., et al., *High-performance supercapacitors based on intertwined CNT/V2O5 nanowire nanocomposites.* Advanced materials, 2011. **23**(6): p. 791-795.

26. Li, Z., et al., *Synthesis and thermal stability of two-dimensional carbide MXene Ti3C2.* Materials Science and Engineering: B, 2015. **191**: p. 33-40.

27. Selima, S., M. Khairy, and M. Mousa, *Comparative studies on the impact of synthesis methods on structural, optical, magnetic and catalytic properties of CuFe2O4.* Ceramics International, 2019. **45**(5): p. 6535-6540.

28. Kewate, O.J. and S. Punniyakoti, *Ti3AlC2 MAX phase and Ti3C2TX MXene-based composites towards supercapacitor applications: a comprehensive review of synthesis, recent progress, and challenges.* Journal of Energy Storage, 2023. **72**: p. 108501.

29. Li, T., et al., *Solid-solid reaction of CuFe2O4 with C in chemical looping system: A comprehensive study.* Fuel, 2020. **267**: p. 117163.

30. Alsafari, I.A., et al., *Synthesis, characterization, photocatalytic and antibacterial properties of copper Ferrite/MXene (CuFe2O4/Ti3C2) nanohybrids.* Ceramics International, 2021. **47**(20): p. 28874-28883.

31. Hu, M., et al., *High-capacitance mechanism for Ti3C2 T x MXene by in situ electrochemical Raman spectroscopy investigation.* ACS nano, 2016. **10**(12): p. 11344-11350.

32. Zhang, W., Y. Xue, and Z. Cui, *Effect of size on the structural transition and magnetic properties of nano-CuFe2O4.* Industrial & Engineering Chemistry Research, 2017. **56**(46): p. 13760-13765.